A novel approach to neutron dosimetry

Matthew J.I. Balmer* and Kelum A.A. Gamage
Department of Engineering, Lancaster University, LA1 4YW, UK

Graeme C. Taylor
Neutron Metrology Group, National Physical Laboratory, Teddington, TW11 0LW, UK
(Dated: May 8, 2016)

Purpose:
Having been overlooked for many years, research is now starting to take into account the directional distribution of neutron workplace fields. Existing neutron dosimetry instrumentation does not account for this directional distribution, resulting in conservative estimates of dose in neutron workplace fields (by around a factor of 2, although this is heavily dependent on the type of field). This conservatism could influence epidemiological studies on the health effects of radiation exposure. This paper reports on the development of an instrument which can estimate the effective dose of a neutron field, accounting for both the direction and the energy distribution.

Methods:
A ^{6}Li-loaded scintillator was used to perform neutron assays at a number of locations in a 20x20x17.5 cm^3 water phantom. The variation in thermal and fast neutron response to different energies and field directions was exploited. The modelled response of the instrument to various neutron fields was used to train an artificial neural network (ANN) to learn the effective dose and ambient dose equivalent of these fields. All experimental data published in this work were measured at the National Physical Laboratory (UK).

Results:
Experimental results were obtained for a number of radionuclide source based neutron fields to test the performance of the system. The results of experimental neutron assays at 25 locations in a water phantom were fed into the trained ANN. A correlation between neutron counting rates in the phantom and neutron fluence rates was experimentally found to provide dose rate estimates. A radionuclide source behind shadow cone was used to create a more complex field in terms of energy and direction. For all fields, the resulting estimates of effective dose rate were within 45% or better of their calculated values, regardless of energy distribution or direction for measurement times greater than 25 minutes.

Conclusions:
This work presents a novel, real-time, approach to workplace neutron dosimetry. It is believed that in the research presented in this paper, for the first time, a single instrument has been able to estimate effective dose.

Keywords: effective dose, ANN, directional neutron survey, Pattern recognition

* m.balmer@lancaster.ac.uk

I. INTRODUCTION

Human exposure to ionising radiation is a health risk which radiation protection practices attempt to reduce. Depending on the type of ionising radiation, a differing risk is experienced. As such, the dose from each type of radiation (such as gamma, neutron, beta) should be considered when assessing this risk.

In neutron dosimetry, the overall risk to the human body is classified as the sum of the risks to individual tissue/organs. However, when considering males and females, they have a different overall risk weighting due to anatomical differences. Furthermore, weighting factors are based on a specific size of human. Depending on the neutron field energy and direction of incidence, the committed dose to each of these organs differs. Therefore, it can be seen that the neutron radiation exposure risk to a human is a complex problem to quantify. Considering these factors, from an instrumentation standpoint, estimating the risk for a specific individual is a difficult, if not currently impossible, task.

The radiation protection quantity *effective dose* can be used to provide an estimation of the health risk due to exposure to a neutron field [1]. Using this quantity, the risk estimate accounts for both the energy distribution and direction of incidence of a neutron field. Using conversion coefficients, a neutron fluence can be transformed into an effective dose for a given incidence of neutron field, by applying fluence to effective dose conversion coefficients that vary with energy and angle [1]. Figure 1 shows how the effective dose coefficients change for antero-posterior (AP), postero-anterior (PA), left-lateral (LLAT) and right-lateral (RLAT) incident radiation. It can be seen that the greatest health risk is experienced with the AP direction of incidence, while the lowest risk is with RLAT incidence.

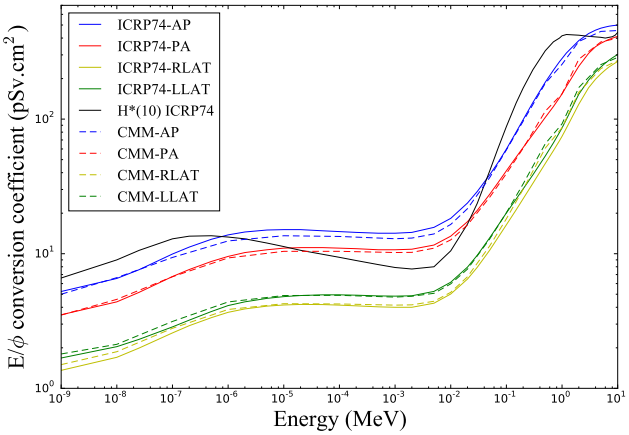

Figure 1. Effective dose coefficients for AP, PA, RLAT, LLAT are shown for both ICRP74 and the Computerised Man Model (CMM) phantom calculated values described in this work (see section 2.2). It can be seen that in some energy regions, *H*(10)* does not always provide a conservative estimate of the AP effective dose.

A number of important points should be noted with regard to effective dose. The ICRP guidelines describe it as something that cannot be measured, and as such, one can only estimate effective dose. Secondly, when considering a workplace field, it is assumed that a single directional component will not dominate. More likely, a complex directional field will result, which will likely vary with neutron energy. As such, using only the published fluence to effective dose conversion coefficients for a limited number of directions, it is a near impossible task to estimate the effective dose of a workplace neutron field with any degree of accuracy.

In light of the practical shortcomings of effective dose, the quantity *ambient dose equivalent H*(10)* is currently used for operational neutron dosimetry. This quantity is supposed to be a conservative measure of the risk, carrying a higher conversion coefficient than the AP fluence to effective dose conversion coefficient. However, it can be seen in Figure 1 that this is not the case for the values currently used in UK industry from ICRP74 [1]. Furthermore, the outcome of radiation health studies are potentially limited by the mostly conservative estimates of the neutron dose. The matter is further complicated by the fact that depending on the field, area survey meters can over read by up to 700% [2]. However, in some measured workplace fields it has been shown that these differences are usually around a factor of 2 [3]. This raises further questions, primarily, what method can be used to validate that an area survey meter is always measuring *H*(10)* more conservatively than effective dose in a workplace field?

It should be noted that ICRP116 provides an updated set of coefficients to reduce this conservatism, however it still falls short in some areas of the spectrum [4, 5]. In this research, the data from ICRP74 have been used, as previous

comparisons of instruments for measuring *H*(10)* have been published using this standard [2].

In this work, the authors have developed a novel instrument to estimate the effective dose of a neutron field. A literature review previously carried out did not find any reference to the existence of an instrument which, from a single location, can estimate effective dose [6]. Recent advances in lithiated plastic scintillators and signal processing techniques now allow both fast and thermal neutron assay to be performed in a single scintillator [7] [8]. It was proposed that by moving this ^{6}Li-loaded scintillator detector within a water phantom and observing the distribution of fast and thermal neutrons within a moderating phantom, an artificial neural network (ANN) could be trained to learn the corresponding effective dose of these fields. The concept of using ANNs to estimate effective dose has previously been investigated with computer simulations [9, 10]. These methods consisted of a single doped scintillator and relied on localising neutron capture within a large scintillator. However, no efficient signal processing methodology was identified to localise neutron capture within a scintillator.

It is believed that in the research presented in this paper, for the first time, a single instrument has been able to estimate effective dose. The instrument has been experimentally tested in multidirectional fields and an error (i.e., the difference between estimated and calculated effective dose rate) of 45% or less was observed when estimating effective dose rate for all fields investigated with a data capture time of 90 minutes or greater.

II. METHODOLOGY

A. Modelling neutron distributions in a water phantom

The initial investigations of this instrument were based around Monte Carlo computer modelling. These set out to understand the distributions of thermal and fast neutrons in a water phantom. A scintillator loaded with 0.14% fractional mass of ^{6}Li, measuring 25 mm diameter and 18 mm thickness was modelled within a water phantom of volume 20x20x17.5 cm^{3}. Individual simulations were performed for a number of different detector locations in the water phantom using Monte Carlo radiation transport package, MCNP v5.0 [11]. For each of these simulations a neutron point source was modelled, which remained at a fixed location 70 cm from the front face of the water phantom. In MCNP, materials were simulated using the ENDF/B-VII.0 neutron cross section tables at temperature 293.13 K. To handle low energy thermal scattering of neutrons below 5 eV, MCNP has thermal treatment for a variety of material types. For s(α, β) thermal treatment, *poly.01t* and *lwtr.01* were included in the MCNP input file, for the scintillator and water respectively. Using the particle tracking file (PTRAC), neutron recoil and neutron capture events within the scintillator were recorded. If an event resulted in a neutron energy deposition of greater than a fixed energy threshold, a fast event was tallied. This threshold was chosen to be the energy region beyond the fixed light production arising from ^{6}Li neutron capture in the scintillator. Further details regarding this can be found in the results section of this work. It was decided to perform the assay at 25 locations on the horizontal plane at the mid-height within the water phantom.

Simulations were performed for 30 minutes of computer time at 25 locations in a 5 x 5 grid pattern in the water phantom. The geometric centre of the scintillator was located at x locations [-7, -3.5, 0, 3.5, 7] and y locations [-7, -3.5, 0, 3.5, 7] (all locations in cm), where 0,0 cm was the centre of the water phantom. For this proof-of-concept instrument, data acquisition for z axis displacements of the detector was not implemented. As such, the training and testing of the instrument does not account for any top or bottom based neutron field directions.

B. Estimating effective dose for a workplace field

To measure the performance of the proposed instrument, a method needed to be identified to calculate the effective dose of an experimental field. Using ICRP published conversion coefficients, doses can be calculated for AP, PA, RLAT, LLAT, ROT and ISO fields. However, this field is assumed to be a parallel beam. Calculating effective dose close to radionuclide neutron sources becomes a difficult task due to the divergent beam nature of the field. Furthermore, in a workplace field, it is anticipated that a complex directional neutron distribution would be present.

Although it may be possible to create rough estimates of the effective dose of a real-world field by attempting to break it down into the above six components, it was decided that values derived from calculations based on an anthropomorphic phantom would better reflect the reality of the workplace. Tom Jordan's Computerised Man Model (CMM) was selected for this purpose as it was listed in the input geometry format of the radiation transport code MCNP [12].

Having completed an initial check on the model, the male phantom was transformed into an hermaphroditic phantom by treating (a) the pectoral muscles as representing breast tissue, and (b) a volume of tissue in front of the spine as representing ovary tissue. F6 (dose) tallies were created for both neutron and photon interactions for each tissue of

interest. A complete list of cells used to approximate the organs and tissues of interest is given in the supplementary material for this work [13]. A number of adjustments to the model were required to observe the agreement shown in Figure 1.

All experimental data published in this work were measured at the National Physical Laboratory (UK) in the low scatter facility [14, 15]. The dimensions of the room were 25x18x18 m^3, with the designated low scatter area being approximately 18x18x15 m^3, and the source was installed close to the centre of this space. For each experimental test performed, a corresponding effective dose at that given location was calculated by modelling the CMM phantom within the low scatter facility.

In order to experimentally synthesise some near-isotropic fields (which could be calculated with confidence against the known scatter characteristics of the room), it was anticipated that a shadow cone in front of a source could be used. The near-isotropic nature of this field was confirmed by inspection of the PTRAC file from MCNP simulations of this setup. However, the shadow cones available formed a shadow in the region of tens of cm, rather than the height of a person. Therefore, to calculate the effective dose behind the shadow cone, the phantom was reduced in scale by a factor of ten, and the density of each tissue increased by a factor of ten. This was in a method analogous to the principles of microdosimetry using tissue equivalent proportional counters [16]. Further details are available in the supplementary material published with this research [13].

C. Artificial neural network approach

Artificial neural networks (ANNs) are well proven for their abilities in pattern recognition systems and have previously been researched for neutron spectrum unfolding purposes [17–21]. Once a neural network has been trained, the network can be deployed into a fast real-time system. It was proposed that by observing the distribution of fast and thermal neutrons within a water phantom, an ANN could be trained to learn the corresponding effective dose of these fields.

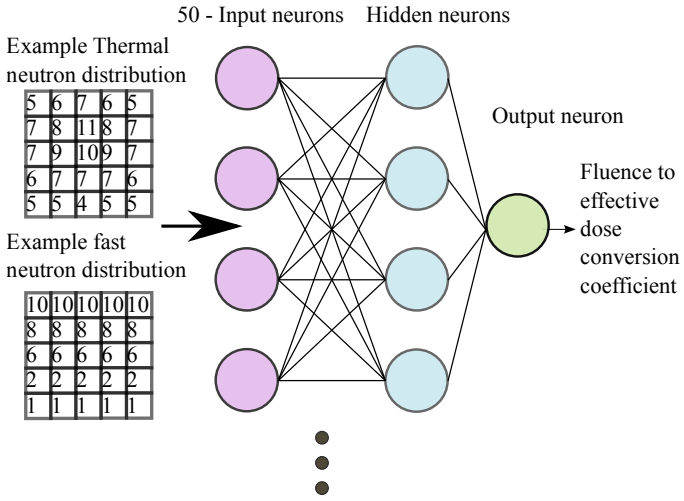

Figure 2. Simplified schematic of the ANN used in this research to estimate the fluence to effective dose conversion coefficient based upon the assayed thermal and fast neutron distributions within a water phantom.

The C based software library FANN, version 2.2.0, was used for the investigations in this work [22]. For ANN training, the resilient propagation (RPROP) learning algorithm has been applied [23], specifically, the iPROP- method [24]. By using individual step sizes for weight updates of each neuron, the RPROP algorithm removes the need for optimisation of a learning rate.

Number of layers, number of neurons and activation functions could all be changed for a given set of input data to optimise the learning of the pattern. The architecture of the network used in this work is shown in Figure 2. The input data consisted of 50 input neurons (fast and thermal neutron assay at 25 locations), feeding into 3 layers of neurons with a sigmoid activation function. The resulting output of the ANN was an estimate of the fluence to effective dose conversion coefficient for the given neutron field.

D. Experimental details

A ^{6}Li-loaded scintillator provided by the Lawrence Livermore National Laboratory (LLNL) was used in this work [7]. The scintillator measured 25 mm in diameter by 18 mm thick (denoted by the LLNL number 9038) and was coupled to an ET Enterprises 9111 PMT with Eljen EJ-550 optical grease. It was then enclosed in a light proof housing. The PMT was housed in an ET Enterprises PDM9111 housing with a C673BFP tapered distribution voltage divider. The high voltage was set to +848 V.

The PMT signal was connected to an Analog Devices AD9254 150 mega-samples-per-second (MS/s), 14 bit analogue-to-digital converter (ADC), located in the control room of the low scatter facility. Low loss, high bandwidth coaxial cable was used to preserve signal quality (Huber + Suhner SX07262BD). Each digitised ADC sample was clocked to an Altera Cyclone IV EP4CE115 field-programmable gate array (FPGA). Further specifications on this digitiser can be found in the authors' previous work [8].

An open top water phantom was used, measuring 20x20x20 cm^3. The water was only filled to a height of 17.5 cm to avoid any spillage during the movement of the detector between assay locations. The PMT was suspended from the top of the water phantom, such that the centre of the scintillator was at a height of 8.75 cm above the bottom of the phantom. The PMT was moved in the X-Y plane by a lead screw on each axis, with each axis supported by a carriage and rail system. Each lead screw was coupled to a 12 V 0.33 A stepper motor with a step angle of 1.8 degrees and a peak holding torque of 2.3 kg/cm. The stepper motors were controlled by an Arduino Uno R3 microntroller board coupled to a motor control PCB. Commands to control the detector location in the water phantom were sent to the microcontroller board from the control room over an Ethernet cable using USB to Ethernet converters at each end of the cable. The instrument as described can be seen in Figure 3.

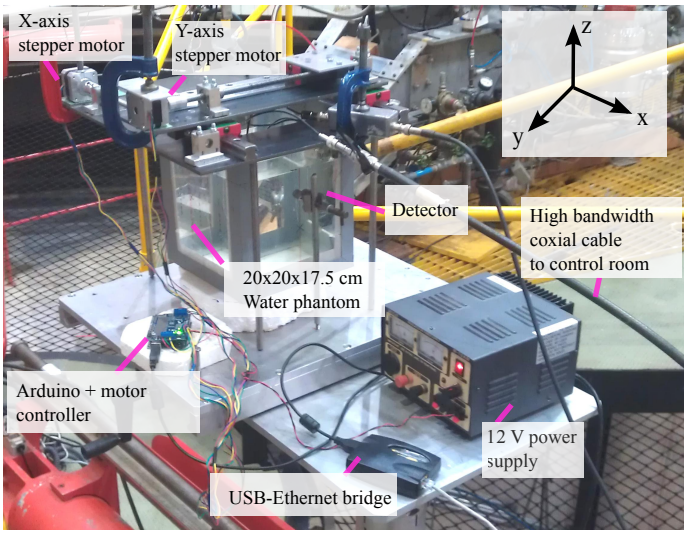

Figure 3. Photograph of the instrument installed in the NPL low scatter facility.

In post processing, the charge comparison method was used to discriminate neutron and gamma interactions in the scintillator [25]. This method compares the total pulse integral (long integral) with the short pulse integral (an area on falling edge of the pulse). The charge comparison method was implemented by summing 32 ADC samples for each pulse to find the long integral. The neutron/gamma discrimination performance of a number of short integrals were investigated, with the best performance given by a value of 10 samples after the peak to the end of the data packet for each pulse. A Gaussian mixtures model was used to perform fast neutron assay, and thermal assay was performed using a peak removal algorithm [8].

III. RESULTS

A. Measuring thermal and fast neutron distributions in a water phantom

For radiation with an AP direction of incidence, the corresponding calculated effective dose conversion coefficients for ^{241}AmBe and ^{252}Cf were 394.7±0.4 and 337.3±0.4 pSv cm^2 respectively. Being comparatively close together in

terms of fluence-dose conversion coefficients, it was decided to see if a difference between these two fields could be observed in terms of fast and thermal neutron distribution in the water phantom. The sources were modelled as an isotropic emission source located 80.5 cm from the centre of the water phantom with a direction of incidence AP. Simulations were run at incremental 1 cm depths along the x axis, with the y and z locations fixed to their respective geometric centres of the water phantom. The modelled distribution of thermal neutrons at varying depths through the water phantom are shown in Figure 4. In the modelled results it can be seen that there was a difference between ^{241}AmBe and ^{252}Cf in the thermal neutron count with an increase in depth into the phantom. It should be noted that these experiments were performed prior to the automatised system being complete, so it is thought that some of these differences could be due to the accuracy of manually positioning the detector.

The modelled results showed promise and were verified experimentally. ^{241}AmBe (NPL serial number 1095) and ^{252}Cf (NPL serial number 4774) sources were exposed to the water phantom at a distance of 80.5 cm, with an AP direction of neutron incidence. The geometric centre of the scintillator was aligned to the mid-height of the water. The scintillator was also aligned to remain fixed in the midpoint of the y axis in the water phantom. Fast and thermal neutron assay was performed at a number of locations along the x axis. The orientation of the axes can be seen in Figure 3. Measurements were performed at each location for 30 minutes.

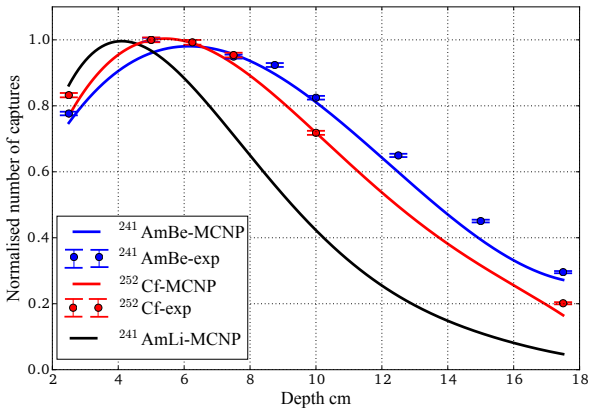

Figure 4. Modelled (denoted by MCNP) and experimental (denoted by "exp") thermal neutron count with a varying assay depth ^{241}AmBe and ^{252}Cf . The dashed lines shown are the experimental results and solid lines the modelled results. The data in each set were normalised to the maximum count across all of the measurement locations in that set. A neutron field with a greater contribution of thermal neutrons (^{241}AmLi) is also shown for comparison.

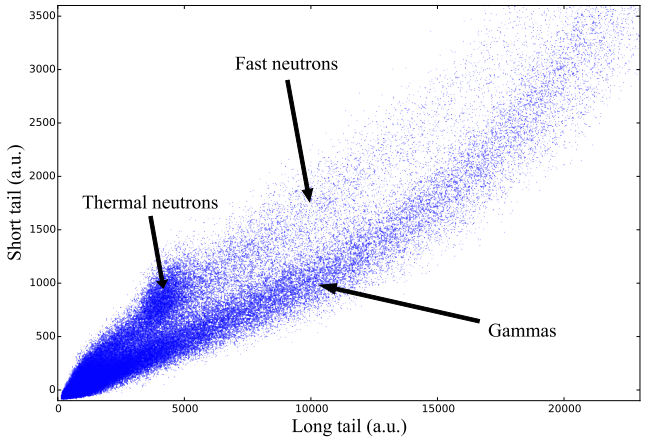

Figure 5. An example of a pulse shape discrimination scatter plot obtained in this work. The thermal and fast neutron regions are shown, as well as the gamma events, which are rejected.

The modelled and experimental thermal neutron distributions can be seen in Figure 4. It can be seen that the experimentally measured thermal distributions closely follow the modelled results for ^{241}AmBe and ^{252}Cf. An ^{241}AmLi

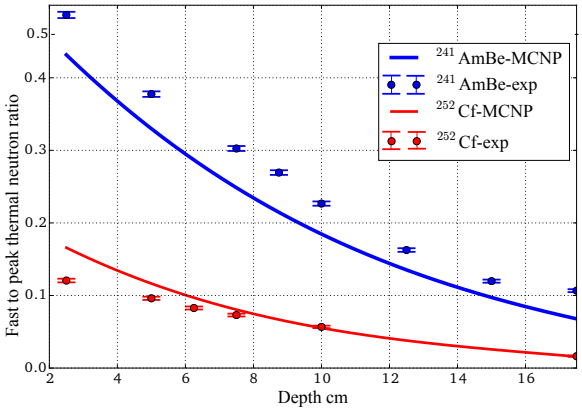

Figure 6. Modelled (denoted by MCNP) and experimental (denoted by "exp") thermal to fast neutron ratio with a varying assay depth for ^{241}AmBe and ^{252}Cf . The dashed lines shown are the experimental results and solid lines the modelled results.

source (dose conversion coefficient of 151.3±0.3 pSv cm^2) was modelled to provide an indication of the difference in distribution that would be observed with a field with a greater contribution of thermal neutrons.

In the experimental results, an event was classified as a fast neutron if it had a greater amplitude than a pulse found in the thermal neutron cluster. An example of a pulse shape discrimination plot, illustrating the fast neutron region and the thermal cluster is shown in Figure 5.

By observing the thermal to fast ratio of the experimental results, the modelled fast neutron threshold (as described in Section II.A) was changed until a close agreement was observed between the modelled and experimental results. This fast neutron threshold was found to be 2.1 MeV in the modelled results. The resulting experimental and modelled thermal to fast neutron ratios distributions, with varying depth, can be seen in Figure 6.

B. Training the ANN

Following the promising agreement between the modelled and experimental neutron distributions in the water phantom, it was decided to train an ANN with a number of simulated neutron field responses of the instrument. Ten different neutron spectra were selected. These were chosen for their range of resulting effective dose conversion coefficients with AP direction of incidence. The highest of these coefficients was 394.7±0.4 pSv cm^2 and the lowest was 9.33±0.02 pSv cm^2. A sample of the neutron spectra used in the ANN training set can be seen in Figure 7. Full details of these fields can be found in the additional supplementary information published for this work [13]. For each field, simulations were performed at 25 locations in the water phantom. For each location, thermal and fast neutron counts were extracted from the simulation.

For each field, training data were obtained for AP, RLAT, PA, LLAT angles of incidence, and the 45 degree angles between each of the these angles. To save computer simulation time, the AP data for each field were rotated to provide a resulting PA, RLAT and LLAT response training set. This same rotation was applied for the 45 degree angle between AP-RLAT to find the remaining responses. Simulations were also performed to find the instrument response to an isotropic field.

The resulting ANN training data contained 90 examples, consisting of 10 fields, with 9 different angles of incidence for each of these neutron spectra. The data for each training example were normalised to the peak value within each set (this peak value being either a fast or thermal neutron count at any one of the assay locations). The output training data were normalised to a conversion coefficient of 600 pSv cm^2. An overview of the data flow within the ANN based system can be seen in Figure 8.

The ANN training was stopped when a total normalised mean squared error of 8x10^{-5} was observed for the complete training set. It was observed that beyond this the ANN started to learn the specific training set too well and performed poorly with data beyond the training set. An optimal setting of 1 hidden layer (with a sigmoid activation function) with 50 hidden neurons was used with the RPROP learning algorithm. Due the random initial weights used in ANN training, each trained network results in a unique output. As such, 10 networks were trained in parallel and the resulting outputs averaged to estimate the fluence to effective dose conversion coefficient. The resulting average ANN results for the training data can be seen in Figure 9.

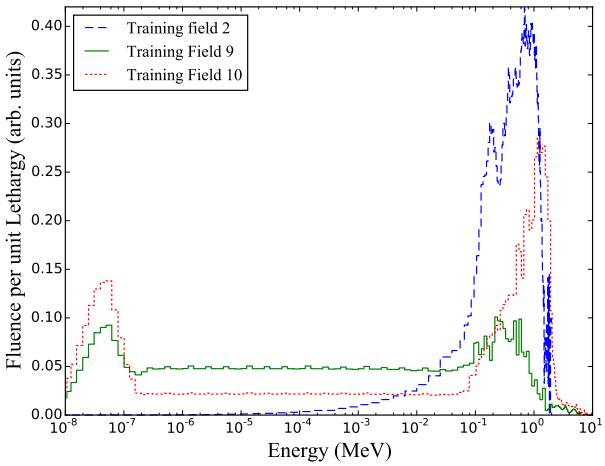

Figure 7. A sample of the workplace-like neutron fields used for performing MCNP simulations to find the instrument response to these fields in terms of thermal and fast neutrons.

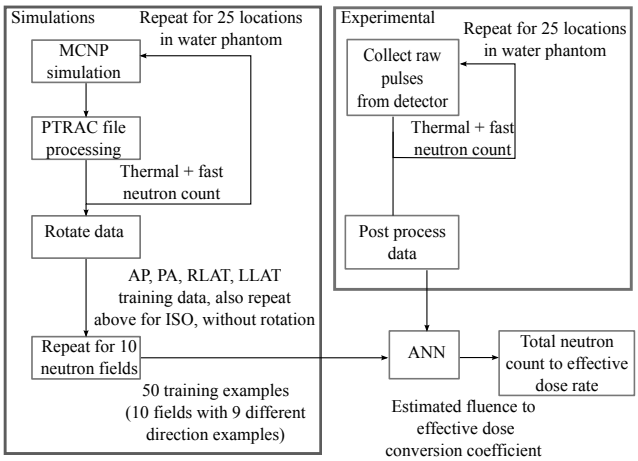

Figure 8. Data flow diagram. The simulated response of the instrument for 10 different neutron fields was used to train an ANN. The experimental results were passed to the trained ANN, resulting in a fluence to effective dose conversion coefficient. This coefficient was converted to an effective dose rate, by applying a conversion factor based on the total number of detected neutron events in the scintillator.

It can be seen in this figure that the network struggled to accurately learn low dose fields with a conversion coefficient of 25 pSv cm^2 or less. It should be noted that two outliers are not shown on this graph. These ANN input values were 4.4 and 7.1 pSv cm^2 respectively which resulted in output errors of 220% and 187% respectively.

C. Single radionuclide source field

It was decided that the first tests for the instrument would be with single radionuclide sources. Although not true to a workplace-like field (in terms of energy or directional components), ^{241}AmBe (for RLAT directions, NPL reference 7245, and for AP, NPL reference 1095), ^{241}AmLi (NPL reference 3250) and ^{252}Cf source (NPL reference 4774) were first selected to test the ANN. These initial experimental results would provide an indication of the performance of the ANN when presented with experimental data for fields and directions it had seen in training. However, distances between source and detector other than 80.5 cm were investigated and the training set did not include the low scatter facility in the model. It was anticipated that room thermalisation of neutrons would produce a slightly different field at the detector, in terms of direction and energy distribution.

A single source was located at the centre of the NPL low scatter facility and the distance to the centre of the

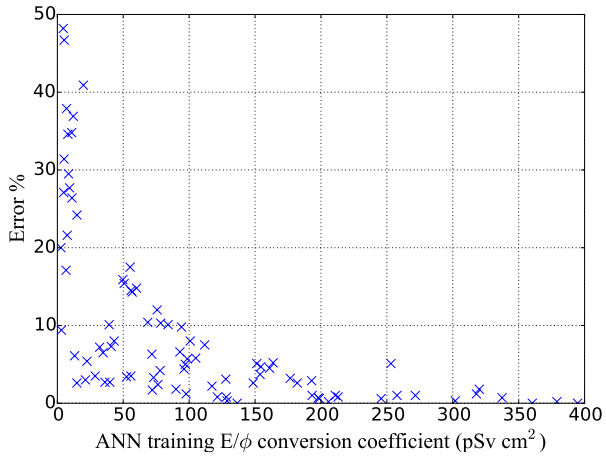

Figure 9. ANN error for the 90 examples, from 10 differen neutron spectra used in training. The error is classified as the percentage difference between the desired and actual output, divided by the desired value, from the average results of 10 ANNs.

detector was recorded. Depending on source activity, differing scan times were chosen. The experimental results for these single source experiments are shown in Table I. The scan time at each individual location within the phantom was kept constant. The time given in Table I is the total time that the FPGA was recording data for at the 25 locations. The resulting ANN fluence to effective dose conversion coefficients were estimated with an error of 38% or better for the 10 experimental measurements performed.

Table I. Experimental results for single radionuclide sources located at a varying distances. The ANN estimated fluence to effective dose (E) conversion coefficient is shown, and the resulting E rate based on the number of detected neutron events within the water phantom.

Neutron Source	Neutron field direction	Scan time (minutes)	Distance to phantom centre (cm)	Fluence to E conversion coefficient (pSv cm^2)			E dose rate (μSv/hr)		
				CMM	ANN	Error	CMM	ANN	Error
^{241}AmBe	AP	400	80.5	384±4	382	1%	41.1±0.4	41.5	0.9%
	AP	750	150.0	349±6	381	9%	10.8±0.4	9.2	15%
	RLAT	750	248.5	182±10	180	1%	17.9±1.4	18.5	3%
^{252}Cf	AP	750	80.5	311±3	295	5%	17.1±0.5	14.1	17%
	AP	9	80.5	311±4	381	23%	17.1±0.5	33.2	94%
	AP	90	80.5	311±3	227	27%	16.4±0.4	13.3	19%
	45°	750	80.5	273±3	170	38%	12.2±0.3	6.7	45%
	AP	285	80.5	311±3	275	12%	16.4±0.4	14.5	11%
^{241}AmLi	AP	1250	150.0	129±3	147	14%	0.36±0.02	0.46	25%
	RLAT	1250	175.7	51±2	48	5%	0.11±0.01	0.11	1%

To calculate the dose rate, a preliminary method was identified for this proof-of-concept instrument. First, the neutron fluence rate at the measured distance for the given neutron emission rate of a source was calculated (these can be found in the supplementary information [13]). Due to the difference in the thermal and fast neutron detection efficiency, a multiplier of 2 was applied to the fast neutron count. These values were found from a fit for which an r^2 value of 0.92 was observed. Further experimental results and optimisation here would likely improve upon this proof-of-concept method.

The sum of the modified fast neutron count and the thermal neutrons detected per second against calculated source emission rate is shown in Figure 10. A fit of y=1.8x was applied to these data. The resulting method for estimating neutron fluence rate is shown in Equation 1.

Table II. Experimental results investigating repeatability of results with a short scan time of 25 minutes. An ^{241}AmBe source was located 248.5 cm from the centre of the phantom at an RLAT angle of incidence.

Observed thermal to fast neutron ratio	Fluence to E conversion coefficient (pSv cm^2)			E rate (μSv/hr)		
	CMM	ANN	Error	CMM	ANN	Error
3.89±0.03	182±10	143	21%	17.9±1.4	17.7	1%
4.09±0.03		182	0.1%		22.1	23%
4.26±0.03		157	14%		18.8	5%
4.63±0.04		166	9%		19.4	8%
4.83±0.04		149	18%		16.9	6%
4.40±0.03		133	27%		15.8	12%
4.34±0.03		143	21%		16.8	6%
4.52±0.04		168	8%		19.5	9%
4.18±0.03		169	7%		20.3	13%
4.45±0.04		159	12%		18.7	5%

$$N_{flu} = \frac{2A_{fast} + A_{thermal}}{t} 1.8 \tag{1}$$

where N_{flu} is the estimated neutron fluence rate at the centre of the water phantom, A_{fast} is the total experimental fast neutron assay in the phantom, $A_{thermal}$ is the total experimental thermal neutron assay in the phantom, t is the total detection scan time, in seconds.

The outlier to the fit shown in Figure 10 is the ^{252}Cf scan for 9 minutes. This is due to shortcomings in the accuracy of the GMM algorithm when small total numbers of pulse have been detected. This is discussed further in the authors' previous work [8]. This estimate of neutron fluence rate(N_{flu}) was multiplied by the ANN estimated conversion (E_{coeff}) coefficient, multiplied by the number of seconds in an hour, to give the resulting dose rate in μSv/hr as shown in Equation 2.

$$E_{rate} = 3600\ N_{flu} E_{coeff} \tag{2}$$

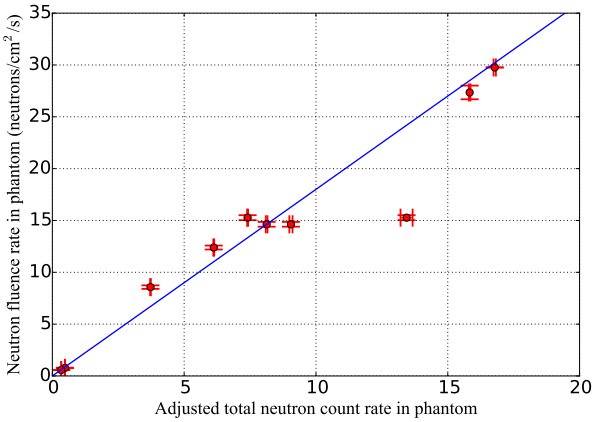

Figure 10. Relationship between the adjusted total neutron count rate in the water phantom and the neutron fluence rate at the given experimental distance for a given source.

In Table I it can be seen that the ANN estimated the conversion coefficient for the short ^{252}Cf scan time with a 23% error, however, the fluence rate estimate resulted in dose rate error of 94%. For longer scan times, the resulting conversion coefficient and dose rate estimates differed by less than 45% between the experimental and calculated values. The largest of these differences being for ^{252}Cf at 45°.

It was decided the poor results from the 9 minute ^{252}Cf scan warranted further investigation of short scan times. With a shorter scan time, the thermal and fast neutron assay has a greater uncertainty. It was decided to perform 10 consecutive data captures with a short scan time (25 minutes) to observe the resulting spread of ANN estimates for ^{241}AmBe (NPL reference 7245) at RLAT angle of incidence. The results can be seen in Table II. Table III shows the averages of the thermal and fast neutron assays at each location within the water phantom for these repeated measurements at the short scan times. The uncertainties are calculated as standard uncertainties.

It can be seen that for a short scan time, the error ranges from 0.1% up to 27%, with a mean error of 14% for the fluence-dose conversion coefficient. This results in an mean error of 9% for the effective dose rate. The measured thermal to fast neutron ratios for these experimental data are shown for comparison in Table II. A ratio of 3.03 was observed at the end of a 750 minute scan with the same experimental setup (as shown in Table I). All ratios in Table II are greater than this ratio. This is thought to be due to an under estimate of the fast neutron content within the field. This suggests that the fast and thermal neutron assay algorithm accuracy for short scan times, will have a tendency to result in an underestimate the effective dose. This hypothesis holds true for the data shown in Table II.

Table III. Averaged (a) thermal and (b) fast neutron assays at each location in the water phantom. These are from 10 consecutive experiments of a short total scan time of 25 minutes for the 25 locations. An ^{241}AmBe source was located 248.5 cm from the centre of the phantom at an RLAT angle of incidence (row 5 (7.0 cm) in the table being closest to the source).

(a)

	-7.0	-3.5	0	3.5	7.0
-7.0	349±25	515±32	650±33	801±33	778±37
-3.5	443±25	652±21	882±30	1041±66	979±41
0	454±26	704±17	935±39	1140±27	1043±21
3.5	454±24	668±25	904±25	1082±24	1032±51
7.0	359±29	524±31	699±21	832±44	838±30

(b)

	-7.0	-3.5	0	3.5	7.0
-7.0	17±12	114±24	153±3	236±10	323±11
-3.5	19±13	121±9	181±9	243±8	341±12
0	37±19	110±20	156±6	244±6	323±8
3.5	40±14	99±23	171±11	232±10	354±7
7.0	7±7	84±23	162±20	241±9	314±8

D. Bidirectional field

With the network having been trained on single directions and isotropic fields, it was decided to see how the instrument performed with two sources located perpendicular to each other. A ^{241}AmLi (NPL reference number 3250) was located AP to the detector at a distance of 144.7 cm. An ^{241}AmBe source (NPL reference number 1152) was located RLAT to the detector at a distance of 195.8 cm. A scan was performed for 1000 minutes. The resulting distribution of thermal and fast neutrons in the water phantom can be seen in the heat plot shown in Figure 11. It is interesting to see the dominance of thermal neutrons suggests an AP source, whilst the fast neutron distribution suggests an RLAT source. The resulting ANN estimated fluence-to-dose conversion coefficient was 180 pSv cm^2 with an error of 6%, shown in Table IV. The dose rate was estimated by the ANN to be 0.93 μSv/hr resulting in an error of 15% with the expected value.

E. Shadow cone field

From the early investigation of this instrument it was known that testing it in a more complex field in terms of energy and direction would be required. However, the field in which the instrument was to be tested must also be understood to know the effective dose of that field. It was decided to synthesise a more complex field with a shadow cone. It was anticipated that this field would create a largely isotropic thermal field with a weak AP component of low angle scattered fast neutrons. A shadow cone (NPL serial number 7) was installed with the front face of the shadow cone 23 cm from the source. The shadow cone was 50 cm long, comprising iron (20 cm) and borated wax (30 cm). The narrow (iron) end had a diameter of 9 cm and the wide (wax) end a diameter of 17 cm, creating an apex angle of 4.57 degrees. The water phantom centre was 150 cm from the source, behind the shadow cone. The effective dose conversion coefficient was calculated to be 91±10 pSv cm^2. Results for two scans, one lasting 1250 minutes and one lasting 25 minutes, can be seen in Table V. The ANN estimated coefficient based on the experimental measurements was 88 pSv cm^2 for a scan time of 1250 minutes. The neutron fluence rate in the detector was calculated based on the fraction of simulated neutrons reaching the detector multiplied by the source neutron emission rate. The resulting ANN effective dose rate was estimated to be 2.9 μSv/hr with a calculated error of 36%. It can be seen that the

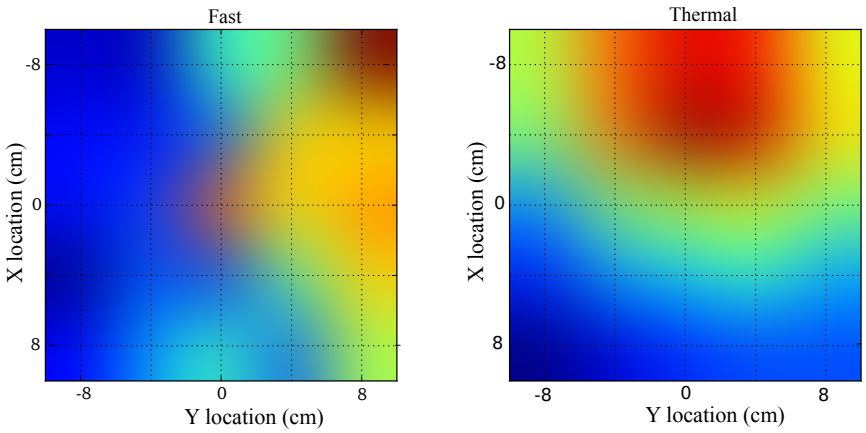

Figure 11. Heat plot of the measured neutron distributions in the water phantom. For (a) fast neutrons (b) thermal neutrons. The dominance of ^{241}AmBe (located RLAT) fast neutrons can be seen in the fast neutron plot. Likewise, the dominance of thermal neutrons from ^{241}AmLi can be seen in the thermal neutron plot.

Table IV. Experimental results with bidirectional field.

Neutron Source	Neutron field direction	Scan time (minutes)	Distance to phantom centre (cm)	Fluence to E conversion coefficient (pSv cm^2)			E rate (μSv/hr)		
				CMM	ANN	Error	CMM	ANN	Error
^{241}AmLi ^{241}AmBe	AP RLAT	1000	144.7 195.8	169±5	180	6%	0.81±0.05	0.93	15%

shorter scan time of 25 minutes resulted in an error of 49% for the effective dose rate. However, further repeated measurements would be required to more fully understand the uncertainty of such a measurement for a short scan time.

Table V. Experimental results with ^{252}Cf behind a shadow cone.

Neutron Source	Neutron field direction	Scan time (minutes)	Distance to phantom centre (cm)	Fluence to E conversion coefficient (pSv cm^2)			E rate (μSv/hr)		
				CMM	ANN	Error	CMM	ANN	Error
^{252}Cf	S/C S/C	25 1250	150.0 150.0	91±10	73 88	20% 3%	4.5±0.6	2.3 2.9	49% 36%

IV. CONCLUSION

In this research a novel approach to neutron dosimetry has been proposed. Performing neutron assays at a number of locations with a ^{6}Li-loaded scintillator detector in a water phantom, a pattern of thermal and fast neutron distributions was observed. An ANN was trained to learn simulated responses of the instrument in 10 different computer simulated fields, each from 9 different directions. The instrument was then experimentally tested in a number of different radiation fields and the effective dose was estimated. When a scan time of greater than 90 minutes was performed, the largest resulting effective dose rate error was found to be 45%. This largest error was an underestimate of the effective dose, and was due to the ANN underestimating the dose. Such underestimates counteract radiological protection principles and large underestimates such as this will require investigation in future work. It should be emphasised, however, that the training data were based purely on computer simulated results. It is thought that the

instrument could be improved with more complex directional fields in training.

This proof-of-concept instrument has shown promise in the experimental testing thus far. However, a significant step forward with this instrument would be the addition of z axis measurements to resolve top and bottom angles of the neutron field. However, this requires considerably more simulations and the ANN would require re-training. Further experimental testing of the instrument in more thermal fields would also beneficial. However, to estimate the effective dose of a neutron field, complex room geometries must be modelled and experimentally verified to gain confidence in the effective dose calculations. Therefore this further testing would need to take place in a facility where this confidence could be gained.

A new set of conversion coefficients were published in ICRP116. Consequently, given that the instrument presented in this research performs the processing within software, changing to ICRP116 recommendations would in theory be a simple software change with no further experimental response characterisations required. However, the same problem with only a limited number of published field directions exists. A complete re-validation of the CMM phantom would be required to obtain ICRP116 based fluence to effective dose conversion coefficients.

It should be noted that the water phantom was investigated for the ease of use in an experimental prototype. However, it is envisaged that a more practical instrument could be realised with polyethylene and multiple compact detectors embedded within a polyethylene cylinder or sphere. A silicon photomultiplier tube coupled to this detector could provide such a compact detector. Using more than one detector would have the benefit of a reduced scan time. A final point, worthy of further future investigation, given that the detector is sensitive to gamma radiation as well as neutron radiation, it is possible that this instrument could be used for gamma dosimetry as well.

ACKNOWLEDGMENTS

The authors would like to express thanks to Natalia Zaitseva and the team at LLNL for providing the scintillator. The authors would like to acknowledge the funding support from EPSRC and the National Physical Laboratory, Teddington, UK. The authors would also like to acknowledge the help and advice of Dr. Nigel Hawkes at the National Physical Laboratory. The authors acknowledge the use of the package Matplotlib for all plots in this research [26]. The data generated in this work are available from the Lancaster University data archive [13].

[1] ICRP, "Conversion Coefficients for use in Radiological Protection against External Radiation," Annals of the ICRP **26**, 35–81 (1996).

[2] R.J. Tanner, C. Molinos, N.J. Roberts, D.T. Bartlett, L.G. Hager, G.C. Taylor, and D.J. Thomas, *Practical Implications of Neutron Survey Instrument Performance*, Tech. Rep. HPA-RPD-016 (Health Protection Agency, Chilton, UK, 2006).

[3] D.T. Bartlett, P. Drake, F. d'Errico, M. Luszik-Bhadra, M. Matzke, and R.J. Tanner, "The importance of the direction distribution of neutron fluence, and methods of determination," Nuclear Instruments and Methods in Physics Research Section A: Accelerators, Spectrometers, Detectors and Associated Equipment **476**, 386 – 394 (2002).

[4] D.J. Thomas, "The system of radiation protection for neutrons: does it fit the purpose?" Radiation Protection Dosimetry **161**, 3–10 (October 2014).

[5] N. Petoussi-Henss, W.E. Bolch, K.F. Eckerman, A. Endo, N. Hertel, J. Hunt, M. Pelliccioni, H. Schlattl, and M. Zankl, "ICRP 116 - Conversion Coefficients for Radiological Protection Quantities for External Radiation Exposures," Annals of the ICRP **40**, 1–257 (2010).

[6] M.J.I. Balmer, K.A.A. Gamage, and G.C. Taylor, "Critical review of directional neutron survey meters," Nuclear Instruments and Methods in Physics Research Section A: Accelerators, Spectrometers, Detectors and Associated Equipment **735**, 7–11 (2014).

[7] N. Zaitseva, A. Glenn, H. Paul Martinez, L. Carman, I. Pawełczak, M. Faust, and S. Payne, "Pulse shape discrimination with lithium-containing organic scintillators," Nuclear Instruments and Methods in Physics Research Section A: Accelerators, Spectrometers, Detectors and Associated Equipment **729**, 747–754 (2013).

[8] M.J.I. Balmer, K.A.A. Gamage, and G.C. Taylor, "Neutron assay in mixed radiation fields with a ^{6}Li-loaded plastic scintillator," Journal of Instrumentation **10**, P08012–1–14 (2015).

[9] G.C. Taylor, "Design of a direction-dependent neutron dosimeter," Radiation Measurements **45**, 1301–1304 (2010).

[10] M.J.I. Balmer, K.A.A. Gamage, and G.C. Taylor, "Detecting energy dependent neutron capture distributions in a liquid scintillator," Nuclear Instruments and Methods in Physics Research Section A: Accelerators, Spectrometers, Detectors and Associated Equipment **776**, 1–7 (2015).

[11] Los Alamos National Laboratory, A General Monte Carlo N-Particle Transport Code, Version 5 (2003).

[12] "Computerized man model," http://cmpwg.ans.org/phantoms.html, accessed: 2015-11-23.

[13] M.J.I. Balmer, K.A.A. Gamage, and G.C. Taylor, "A novel approach to neutron dosimetry [dataset]," DOI: 10.17635/lancaster/researchdata/56.

[14] O.F. Naismith and D.J. Thomas, "MCNP Calculation of Neutron Scatter in the Main Bay of the Chadwick Building, NPL," NPL Report - CIRA004 (1996).

[15] G.C. Taylor and D.J. Thomas, "Neutron scatter characteristics of the low-scatter facility of the Chadwick Building, NPL," NPL Report - CIRM17 (1998).

[16] ICRU, "Microdosimetry - ICRU report 36," International Commission on Radiation Units and Measurements - report 36 (1983).

[17] R. Koohi-Fayegh, S. Green, N.M.J. Crout, G.C. Taylor, and M.C. Scott, "Neural network unfolding of photon and neutron spectra using an NE-213 scintillation detector," Nuclear Instruments and Methods in Physics Research Section A: Accelerators, Spectrometers, Detectors and Associated Equipment **329**, 269–276 (May 1993).

[18] M.R. Kardan, S. Setayeshi, R. Koohi-Fayegh, and M. Ghiassi-Nejad, "Neutron spectra unfolding in Bonner spheres spectrometry using neural networks," Radiation Protection Dosimetry **104**, 27–30 (April 2003).

[19] S. Avdic, S.A. Pozzi, and V. Protopopescu, "Detector response unfolding using artificial neural networks," Nuclear Instruments and Methods in Physics Research Section A: Accelerators, Spectrometers, Detectors and Associated Equipment **565**, 742–752 (2006).

[20] A. Sharghi Ido, M.R. Bonyadi, G.R. Etaati, and M. Shahriari, "Unfolding the neutron spectrum of a NE213 scintillator using artificial neural networks," Applied Radiation and Isotopes **67**, 1912–1918 (2009).

[21] J.M. Ortiz-Rodríguez, A. Reyes Alfaro, A. Reyes Haro, J.M. Cervantes Viramontes, and H.R. Vega-Carrillo, "A neutron spectrum unfolding computer code based on artificial neural networks," Radiation Physics and Chemistry **95**, 428–431 (2014).

[22] S. Nissen, "Implementation of a Fast Artificial Neural Network library (FANN)," (2003).

[23] M. Riedmiller and H. Braun, "A direct adaptive method for faster backpropagation learning: The RPROP algorithm," in *IEEE International Conference on Neural Networks, 1993* (IEEE, 1993) pp. 586–591.

[24] C. Igel and M. Hüsken, "Empirical evaluation of the improved rprop learning algorithms," Neurocomputing **50**, 105 – 123 (2003).

[25] T.K. Alexander and F.S. Goulding, "An amplitude-insensitive system that distinguishes pulses of different shapes," Nuclear Instruments and Methods **13**, 244–246 (October 1961).

[26] J.D. Hunter, "Matplotlib: A 2D graphics environment," Computing in Science and Engineering **9**, 90–95 (June 2007).